

LC4-DViT: Land-cover Creation for Land-cover Classification with Deformable Vision Transformer

Kai Wang^{*}, Siyi Chen^{*}, *Student Member, IEEE*, Weicong Pang^{*}, Chenchen Zhang, Renjun Gao, Ziru Chen, Cheng Li[†], *Student Member, IEEE*, Dasa Gu[†], Rui Huang[†], and Alexis Kai Hon Lau

Abstract—Land-cover underpins ecosystem services, hydrologic regulation, disaster-risk reduction, and evidence-based land planning; timely, accurate land-cover maps are therefore critical for environmental stewardship. Remote sensing-based land-cover classification offers a scalable route to such maps but is hindered by scarce and imbalanced annotations and by geometric distortions in high-resolution scenes. We propose LC4-DViT (Land-cover Creation for Land-cover Classification with Deformable Vision Transformer), a framework that combines generative data creation with a deformation-aware Vision Transformer. A text-guided diffusion pipeline uses GPT-4o-generated scene descriptions and super-resolved exemplars to synthesize class-balanced, high-fidelity training images, while DViT couples a DCNv4 deformable convolutional backbone with a Vision Transformer encoder to jointly capture fine-scale geometry and global context. On eight classes from the Aerial Image Dataset (AID)—Beach, Bridge, Desert, Forest, Mountain, Pond, Port, and River—DViT achieves 0.9572 overall accuracy, 0.9576 macro F1-score, and 0.9510 Cohen’s Kappa, improving over a vanilla ViT baseline (0.9274 OA, 0.9300 macro F1, 0.9169 Kappa) and outperforming ResNet50, MobileNetV2, and FlashInternImage. Cross-dataset experiments on a three-class SIRI-WHU subset (Harbor, Pond, River) yield 0.9333 overall accuracy, 0.9316 macro F1, and 0.8989 Kappa, indicating good transferability. An LLM-based judge using GPT-4o to score Grad-CAM heatmaps further shows that DViT’s attention aligns best with hydrologically meaningful structures. These results suggest that description-driven generative augmentation combined with deformation-aware transformers is a promising approach for high-resolution land-cover mapping. The project is available at [here](#).

Index Terms—Remote sensing, image diffusion, land-cover classification, deformable convolution network, vision transformer.

I. INTRODUCTION

Land-cover is a foundational descriptor of the Earth’s surface that shapes ecosystem services, biodiversity, carbon storage, hydrologic regulation, food security, and urban sustainability at global scales [1]. Accurate, timely land-cover maps

are therefore essential for environmental monitoring, spatial planning, and policy-capturing the dynamics of urbanization and agriculture as well as safeguarding water bodies and wetlands that deliver critical cooling, purification, and ecological functions [2]–[5]. Remote sensing-based scene classification provides a scalable path to such maps and has advanced rapidly with deep learning [6], [7]; yet practical deployment remains hampered by scarce and imbalanced annotations and by the difficulty of modeling irregular [8], deformation-rich landforms in high-resolution imagery [9]–[11].

Diffusion-based generative modeling has rapidly progressed from synthesizing natural photographs to more complex modalities such as art style transfer, super-resolution, and video creation [12]–[14]. Early work established denoising-diffusion probabilistic models as a stable, high-fidelity alternative to GANs [15]–[19], enabling photo-realistic imagery and text-to-image systems such as GLIDE [20] and Imagen [21]; parallel advances have extended the paradigm to video, where cascaded architectures sequentially denoise spatio-temporal volumes with impressive realism. Within remote sensing, adaptation has been comparatively recent: RSDiff [22] introduced a two-stage cascade for text-conditioned satellite scenes, SatDM [23] and DiffusionSat [24] injected semantic masks or metadata to guide layout, and the latest CRS-Diff [25] incorporates multi-condition control (text, metadata, sketches) to improve geographic consistency and downstream utility. Despite these gains, most pipelines still rely on generic prompts and ad-hoc filtering [26], yielding artifacts that limit their value for high-precision tasks. Motivated by these gaps, our work couples GPT-4o-generated [27], class-specific descriptions with exemplar-conditioned Stable Diffusion and rigorous perceptual gating, producing high-fidelity, deformation-rich samples tailored for land-cover applications.

Land-cover mapping has progressed from early pixel-wise statistical classifiers to modern deep-learning pipelines, yet several structural bottlenecks remain [28], [29]. Convolutional neural networks (CNNs) fine-tuned from natural-image backbones have dominated recent benchmarks and achieved impressive gains in scene-level accuracy [30]–[37]; however, their fixed, square receptive fields struggle with the elongated shorelines, meandering rivers, and fragmented urban parcels that typify high-resolution remote-sensing imagery [38]–[40]. Transformer variants introduce global self-attention and have reduced spectral-spatial aliasing [41], [42], but most implementations still assume regularly sampled grids and require dense, task-specific supervision that is costly to acquire. Transfer learning and self-supervised strategies alle-

Kai Wang, Siyi Chen, Weicong Pang, Chenchen Zhang, Ziru Chen, Cheng Li, Dasa Gu and Alexis Kai Hon Lau are with The Hong Kong University of Science and Technology.

([†] Corresponding author: Cheng Li; Dasa Gu; Rui Huang; Corresponding e-mail: clieo@connect.ust.hk (Cheng Li).)

Kai Wang and Rui Huang are with The Chinese University of Hong Kong, Shenzhen.

Siyi Chen is with The Johns Hopkins University.

Weicong Pang is with the National University of Singapore.

Renjun Gao is with Macau University of Science and Technology.

* Kai Wang, Siyi Chen and Weicong Pang contributed equally to this work.

This work has been submitted to the IEEE for possible publication. Copyright may be transferred without notice, after which this version may no longer be accessible.

viate data scarcity to a degree [43]–[45], yet performance remains capped by the long-tailed, class-imbalanced nature of real-world aerial datasets and by cross-sensor domain shifts. Parallel work in diffusion-based generation has begun to synthesize auxiliary satellite scenes (e.g., RSDiff [22], SatDM [23], DiffusionSat [24]) to enrich training corpora; nevertheless, these pipelines rely on generic prompts and heuristic filtering, often yielding semantic inconsistencies and geometric artifacts that limit downstream utility [26]. In short, existing land-use/land-cover (LULC) classifiers (i) model complex landform geometries with inflexible kernels or (ii) augment data with imagery whose fidelity is insufficient for fine-grained mapping, leaving a gap that the present LC4-DViT framework seeks to close by uniting class-balanced, description-driven diffusion sampling with a deformation-aware Vision Transformer.

To make these challenges concrete, we deliberately design our experimental setting around hydrology- and infrastructure-related land-cover types, where errors are both frequent and costly. In practice, narrow rivers, small ponds, beaches, ports, and bridges occupy only a tiny fraction of a scene, exhibit highly elongated and deformable geometries, and are embedded within visually confounding surroundings such as dense urban fabric, desert, forest, or mountainous terrain. We therefore select a subset of AID classes—Beach, Bridge, Desert, Forest, Mountain, Pond, Port, and River—and their counterparts in SIRI-WHU (Harbor, River, Pond) as a focused testbed. Together, these categories trace a simplified surface water cycle from upland mountains and forested catchments, through arid transition zones, to rivers, small inland water bodies, and coastal/port areas, linking directly to applications in flood-risk assessment, blue-green infrastructure planning, and urban heat mitigation. At the same time, their strong class imbalance and complex geometries provide a stringent stress test for both our diffusion-based land-cover creation pipeline and the deformation-aware DViT classifier, ensuring that any performance gains are demonstrated on some of the most challenging yet practically important LULC types. This study propose an integrated land-cover mapping framework that simultaneously tackles data scarcity and geometric complexity by coupling description-driven diffusion-based land-cover creation with a deformation-aware Vision Transformer for downstream classification. Existing diffusion models for remote sensing imagery [22]–[25] and deformable or Transformer-based classifiers [42], [56], [58] address generation and recognition largely in isolation, without a unified, systematically evaluated pipeline targeted at hydrology- and infrastructure-related LULC classes.

This work makes the following innovations to remote sensing mapping and geospatial AI fields:

- *Data-centric advance.* We introduce a prompt- and structure-aware diffusion pipeline (Real-ESRGAN pre-enhancement + GPT-4o descriptions + ControlNet guidance) that produces class-balanced, high-fidelity land-cover images, directly mitigating annotation scarcity and long-tailed imbalance in aerial datasets.
- *Model-centric advance.* We propose a deformation-aware Vision Transformer (DViT) that couples DCNv4’s adaptive

receptive fields with ViT’s global context, explicitly targeting irregular, deformation-rich landforms (e.g., meandering rivers, bridges, ports) that defeat fixed-kernel CNNs.

- *Verified efficacy across diverse backbones.* On eight AID classes, LC4-DViT achieves 0.9572 overall accuracy, 0.9592 mean accuracy, 0.9510 Cohen’s Kappa, and 0.9576 macro F1, improving over a vanilla ViT baseline by 2.98 (OA), 2.86 (mAcc), and 3.41 (Kappa) percentage points and outperforming three strong non-deformable backbones—FlashInternImage, ResNet50, and MobileNetV2—without increasing model size (Table II and Fig. 3).
- *Cross-dataset validation and interpretability.* On a SIRI-WHU subset (Harbor, Pond, River), DViT attains 0.9333 overall accuracy, 0.9316 macro F1, and 0.8989 Kappa, surpassing all four baselines and demonstrating cross-dataset generalization. We further introduce an LLM-based judge, where GPT-4o evaluates Grad-CAM attention heatmaps for how well they focus on hydrologically meaningful regions; across all classes, DViT receives the highest alignment scores, corroborating its superior spatial reasoning.
- *Practical impact and extensibility.* By boosting recognition of hydrological and infrastructure classes critical to environmental monitoring and land planning, the pipeline reduces labeling cost and is plug-and-play for multi-/hyper-spectral inputs and cross-sensor deployments, facilitating transfer to broader geographies and sensors.

In response to these challenges, we introduce LC4-DViT (Land-cover Creation for Land-cover Classification with Deformable Vision Transformer), an end-to-end framework designed to enhance land-use classification by combining land-cover creation and deformable Vision Transformers. The first module utilizes the RRDBNet model within the Real-ESRGAN framework [47], [48] for super-resolution processing, because many high-resolution tiles are still affected by compression, resampling, and sensor blur, and small hydrological structures such as narrow channels or bridge decks are easily lost at native resolution. Enhancing spatial detail before generation supplies both GPT-4o and ControlNet with sharper boundaries and edges, leading to more realistic and structurally consistent synthetic scenes. Then, GPT-4o is employed to generate textual descriptions based on each class of land cover in remote sensing images. These textual descriptions, along with the original images, are used in combination with Stable Diffusion to generate new samples for data augmentation, explicitly targeting minority classes and rare geometric configurations that are underrepresented in the original corpus. The second module introduces the DViT model for land-cover classification of remote sensing images. DViT utilizes the DCNv4 backbone to extract spatially rich features, which are then processed through a Vision Transformer to capture global context and interpatch relationships. The integration of deformable convolutions enables dynamic adaptation to complex spatial patterns, so that the classifier can fully exploit the additional geometric diversity introduced by the generative pipeline. This staged design—from super-resolution, to controlled diffusion-based sample creation, to deformation-aware classification—closely mirrors the main failure modes of existing LULC pipelines and addresses them in a principled,

modular fashion.

The structure of this paper is organized as follows. Section II introduces the data and the proposed framework. Section III presents the experimental analysis. Section IV discusses the significance, limitations, and future work. Section V concludes the paper.

II. MATERIALS AND METHODOLOGY

A. Dataset

The study uses the Aerial Image Dataset (AID), a comprehensive large-scale remote sensing dataset designed to facilitate aerial scene classification in the domain of remote sensing [32]. It was constructed by collecting over ten thousand high-resolution aerial images sourced from Google Earth imagery, processed from original optical aerial photos using RGB renderings. Although the images are derived from Google Earth, studies have shown that there is negligible difference between these images and real optical aerial photographs—even at the pixel level—making them suitable for scene classification tasks. In this work, we focus on eight AID scene categories, Beach, Bridge, Desert, Forest, Mountain, Pond, Port, and River—selected to emphasize hydrologically relevant environments. Specifically, Beach and River capture dynamic shoreline and fluvial corridors, Pond represents still-water bodies, and Port and Bridge model human-water interfaces critical to urban water management; Desert, Forest, and Mountain serve as geomorphic and land-cover contrasts that influence runoff generation, watershed connectivity, and water availability. Together, these categories span diverse geographic regions and environments, enabling robust model evaluation for applications such as water-resource monitoring and urban planning [32]. This dataset therefore serves as an essential benchmark for the development and comparison of scene-classification algorithms.

To further validate the effectiveness of our DViT model and assess cross-dataset generalization, we additionally evaluate on the SIRI-WHU dataset using the Harbor, River, and Pond classes. SIRI-WHU is a high-resolution remote-sensing scene dataset widely used for aerial scene classification [46], providing standardized categories that complement AID and enable an external check on model robustness.

For the AID dataset, this work uses all the eight scene categories images comprising 2860 images. We first split the original images into train, valid, and test datasets with approximate 8:1:1 ratio, stratified by class. Super-resolution and text-guided image diffusion are then applied only to the original train dataset, generating one super-resolved image and two diffusion-based images for each training sample. The original valid and test datasets are merged to form the final, non-augmented test dataset, while the union of the original training images and their augmented counterparts is randomly divided into a new training/validation split with an 8:2 ratio, again in a class-balanced manner. This results in a total of 10,003 images (original images + generation images), including 7,552 images for training, 1,914 for validation, and 537 for testing.

For the SIRI-WHU dataset, this work uses all the three scene categories images, comprising 600 images. The dataset is split

into train, valid, and test datasets using the ratio of 8:1:1, and the same proportion is maintained within each class. No super-resolution or diffusion-based augmentation is applied, and all experiments on SIRI-WHU use the original images only.

B. LVC2-DViT Framework

The LC4-DViT framework is designed to enhance remote sensing land-use classification by combining advanced data augmentation techniques and deformation-aware classification models. It consists of three main modules. The first module employs the RRDBNet model within the Real-ESRGAN framework for super-resolution and the second part uses GPT-4o to generate textual descriptions for land-cover classes, which are then combined with Stable Diffusion to create augmented samples. The third module integrates our proposed DViT model for land-cover classification, improving accuracy by handling complex landform geometries. The architecture of the pipeline is illustrated in Figure 1.

C. Image Super-Resolution

For enhancing the resolution and detail of the aerial imagery used in our study, we apply super-resolution to all images. Specifically, we employ the RRDBNet model within the Real-ESRGAN framework [47], chosen for its strong performance in upscaling low-resolution images while maintaining fine details and minimizing artifacts [48]. The configuration uses 23 residual blocks and performs $4 \times$ upscaling, improving image resolution while preserving critical features for accurate scene classification and maintaining computational efficiency for downstream processing.

D. Image Diffusion

A GPT-4o-assisted Stable Diffusion pipeline is adopted to enlarge the training corpus with high-fidelity remote-sensing imagery while avoiding the monotonicity that characterizes conventional augmentation techniques. First, GPT-4 analyzes each original AID image and produces a detailed Stable-Diffusion-style prompt that faithfully describes its semantic content [49]. These prompts are structured according to the standard weighting order used in Stable Diffusion, incorporating elements such as viewpoint, scene composition, and image type. These prompts serve as positive textual conditions for a latent diffusion model, Stable Diffusion [50], thus generating additional samples that preserve key attributes of the scene. Because the vanilla Stable Diffusion model, trained on generic internet photographs, may yield outputs with artistic or cartoon-like artifacts, a domain-adapted variant fine-tuned on landscape imagery is employed, together with a “snapshot photo realism” LoRA module to reinforce photorealistic style [51], [52]. Complementary negative prompts further suppress painterly textures, ensuring that the synthesized images resemble authentic aerial photographs suitable for land-cover analysis.

To retain essential spatial structure, the generation process is guided by ControlNet [53]. Canny edge maps extracted from each source image delineate salient objects, rivers, bridges,

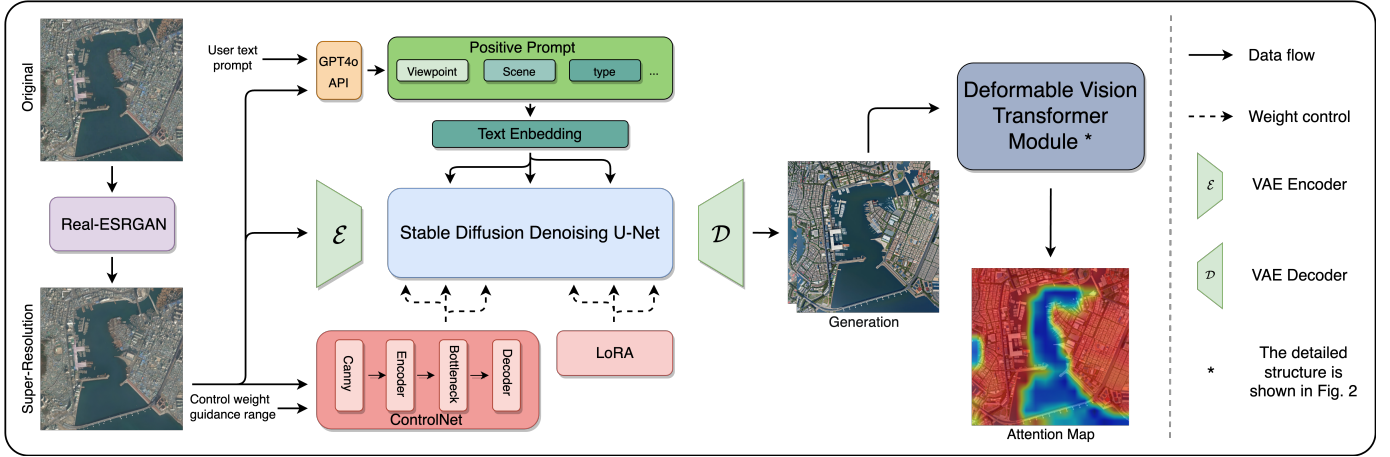


Fig. 1. Overall architecture of LC4-DViT. The pipeline first enhances low-resolution remote sensing images using RRDBNet within the Real-ESRGAN framework, and then leverages GPT-4o-generated land-cover descriptions together with Stable Diffusion to synthesize diverse augmented samples. Finally, the proposed deformation-aware ViT (DViT) module performs land-cover classification by explicitly modeling complex landform geometries, resulting in improved robustness and accuracy.

and beaches and are supplied as auxiliary conditions to the diffusion model. With a narrow edge-detection threshold and adequate guidance steps, ControlNet constrains modifications to peripheral regions while preserving the core geometry of target features. Such structurally aware augmentation aligns with recent diffusion-based methods that enforce spatial consistency in remote-sensing synthesis [51], [54], [55], and it supplies the LC4-DViT classifier with diverse yet credible training examples, ultimately enhancing mapping performance.

E. Resnet50

The ResNet-50 architecture [72] is a deep convolutional backbone that leverages residual learning to ease the optimization of very deep networks and improve representational capacity. It reformulates each building block to learn a residual function with respect to the input via identity shortcut connections, enabling gradient flow across many stacked layers and effectively mitigating the degradation problem observed in plain deep networks. Structurally, ResNet-50 adopts a bottleneck design composed of 1×1 , 3×3 , and 1×1 convolutions, where the first and last 1×1 layers reduce and restore channel dimensions to keep computational cost manageable while allowing the network to reach 50 layers and beyond. This design yields substantially higher accuracy than VGG-style [75] architectures at comparable or lower floating point operations, achieving strong ImageNet classification performance and demonstrating excellent transferability as a generic backbone for object detection and semantic segmentation benchmarks such as Faster R-CNN [74] on PASCAL VOC [76] and MS COCO [77].

F. MobileNetV2

MobileNetV2 [73] is a lightweight convolutional architecture specifically tailored for mobile and resource-constrained scenarios, designed to provide a favorable trade-off between accuracy, parameter count, and computational cost. Its core building block is the inverted residual with linear bottleneck,

which first expands a low-dimensional representation to a higher-dimensional space, applies depthwise separable convolutions to model spatial correlations efficiently, and then projects back to a compact, linear bottleneck to preserve information while avoiding destructive nonlinearities in low-dimensional spaces. Combined with width multipliers and adjustable input resolutions, this design allows MobileNetV2 to span a spectrum of model sizes with multiply-adds ranging from only a few million to several hundred million operations, while remaining competitive with heavier backbones on ImageNet [59] classification. Furthermore, when integrated with SSDLite [80] for detection and a reduced DeepLabv3 [79] head for semantic segmentation, MobileNetV2 delivers efficient yet accurate performance on COCO [77] and PASCAL VOC [76], making it a strong baseline backbone for land-use classification tasks under strict latency and memory constraints.

G. FlashInternImage

The FlashInternImage framework serves as an advanced visual backbone for our land-use classification tasks. At the core of this architecture is Deformable Convolution v4 (DCNv4) [56], which significantly improves upon traditional convolutional and attention-based methods by integrating adaptive aggregation windows and dynamically adjustable weights. DCNv4 addresses previous limitations by eliminating the softmax normalization in spatial aggregation, thus improving expressivity while simultaneously optimizing memory access to reduce computational redundancy and enhance inference speed. Compared to DCNv3 [57], DCNv4 achieves over three-fold acceleration in forward computation and substantially faster convergence. Consequently, integrating DCNv4 into the InternImage [58] architecture, resulting in FlashInternImage, provides an impressive 80% speed increase without compromising, and even further improving, overall performance across various vision tasks. FlashInternImage adopts a hierarchical multi-stage architecture, and the input image initially

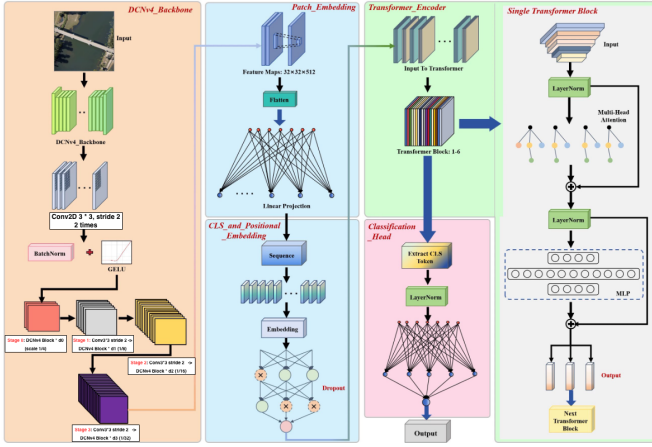


Fig. 2. Overall architecture of the proposed Deformable Vision Transformer (DViT).

undergoes preliminary feature extraction via a stem layer, subsequently processed by multiple InternImage blocks, each incorporating DCNv4 layers, multilayer perceptron (MLP) layers, and normalization operations. These blocks progressively capture both local and global spatial dependencies at increasing semantic abstraction levels. Ultimately, features are aggregated through adaptive pooling, followed by fully connected layers to achieve accurate classification. FlashInternImage has demonstrated exceptional results across diverse vision benchmarks, such as image classification (achieving up to 88.1% accuracy on ImageNet-22K [59]), instance segmentation on the COCO benchmark [60], and semantic segmentation on the ADE20K benchmark [61], highlighting its superior capability and robustness in managing geometric complexities inherent in high-resolution remote sensing imagery.

H. Vision Transformer

The Vision Transformer (ViT) [62] is a classical computer-vision model for classification tasks that partitions the input image into nonoverlapping patches and linearly maps each patch to a vector of the same dimension. These patch embeddings are concatenated with a learnable classification token and position encoding to form a sequence. Only the encoder stack of the Transformer is used for end-to-end feature extraction. Each layer applies LayerNorm, multihead self-attention, and a residual connection, followed by another LayerNorm, a two-layer feedforward network (FFN), and another residual connection. The representation of the classification token is passed to an MLP head to produce class distributions. ViT has achieved better classification accuracies compared with traditional CNNs. However, the complexity of its self-attention calculation increases greatly with the number of patches and it is insensitive to local deformations. This motivates us to integrate deformable convolutional networks into its architecture.

I. Deformable Vision Transformer

Deformable Vision Transformer (DViT) is a hybrid computer-vision architecture specifically designed for remote

sensing land-use classification, effectively integrating fine-grained spatial information with global contextual representations [63]. The model is built upon a DCNv4-based hierarchical backbone in the style of FlashInternImage to leverage dynamic and adaptive spatial modeling capabilities and a ViT-style Transformer encoder. DCNv4 specializes in handling complex geometric variations in images through its deformable convolution mechanisms, while ViT excels at capturing global contextual dependencies through self-attention mechanisms. DViT adapts these two models by concentrating on combining their complementary strengths, employing DCNv4’s robust local adaptive feature-extraction capabilities in the convolutional backbone and ViT’s ability to model long-range dependencies in its Transformer encoder. This adaptation ensures that the network can effectively capture both fine-grained spatial details and global contextual information, significantly enhancing the accuracy and generalizability of remote sensing land-use classification tasks.

The overall architecture of the DViT framework is shown in Fig. 2. The workflow can be delineated into four distinct stages. First, the input remote sensing image is processed by a DCNv4 backbone designed in a hierarchical, InternImage-style fashion. A lightweight convolutional stem with Batch-Norm and GELU activations progressively downsamples the image to one quarter of the original resolution using two stacked 3×3 convolutions with stride 2. The backbone then applies four consecutive DCNv4 stages operating on feature maps at $1/4$, $1/8$, $1/16$, and $1/32$ of the input size. The first stage reuses the $1/4$ -resolution features from the stem, while the subsequent stages start with a 3×3 convolutional downsampling layer (stride 2) followed by several DCNv4 blocks. Within each DCNv4 block, the feature sequence is normalized with LayerNorm, refined by a DCNv4 operator with learnable offsets, and then further transformed by an MLP. Both the DCNv4 and MLP branches are equipped with residual connections, optional layer-scale parameters, and DropPath, enabling stable optimization of deeper deformable hierarchies. This backbone produces compact but information-rich feature maps with progressively increased channel dimensions. Subsequently, these feature maps undergo patch embedding, where they are flattened and linearly projected into a high-dimensional embedding space. Meanwhile, the model incorporates a learnable classification token (CLS) and positional embeddings, preserving positional information and enabling the network to discriminate patches based on their spatial arrangement. These embeddings are then fed into the Transformer encoder, consisting of several Transformer blocks. Each block comprises multihead self-attention mechanisms and feedforward neural networks with residual connections, effectively modeling interpatch relationships. Finally, the classification head extracts the output corresponding to the CLS token, normalizes it via layer normalization, and utilizes a fully connected layer to predict the final class labels.

The essence of DViT lies in its unique integration of adaptive convolutional processing and Transformer-based global contextual understanding, clearly differentiating it from existing hybrid models such as RoadFormer [42]. The main advantages of DViT can be summarized as follows:

TABLE I
IMAGE QUALITY EVALUATION USING KID METRICS.

Method	Dataset	KID ↓
LVC-DViT (Ours)	AID	12.10
UniControl	CNSATMAP	20.42

- DViT leverages the DCNv4 backbone’s powerful deformable convolution capability, dynamically adapting receptive fields to capture intricate spatial relationships effectively, thereby overcoming challenges like occlusions, rotations, and complex geometric distortions prevalent in remote sensing imagery.
- The carefully designed transition from convolutional feature maps to Transformer embeddings, incorporating positional and classification tokens, enhances the network’s sensitivity to spatial context and positional variance.
- The use of a Transformer encoder enables DViT to comprehensively model global interdependencies among image patches, addressing the limitations of convolution-only methods that typically neglect long-range interactions.
- The extensive use of normalization and dropout layers within both convolutional and Transformer modules significantly improves the training stability and generalization capacity of the model, ensuring robust performance across diverse remote sensing scenarios.

III. RESULTS

A. Environment Setup

The experimental component of this study was conducted using Python 3.12 and the PyTorch framework. The experiments were carried out on hardware equipped with NVIDIA RTX 4090. To ensure the reliability and stability of our findings, each model underwent ten separate experimental runs for comparison. This approach allowed for a more comprehensive assessment of the models’ performance and stability across different experimental conditions.

B. Evaluation of Diffusion Framework

To assess the quality of the generated images, we employed two commonly used metrics: Kernel Inception Distance (KID). The KID metric evaluates the distributional similarity between the features of the generated and original images, with lower values indicating closer similarity [64]. For our evaluation, the generated images were compared to their corresponding original images, resulting in an average KID score of 12.1, suggesting a reasonable alignment with the original data. While KID suggest room for improvement, the current strategy of the framework provides satisfactory results, demonstrating its capability in generating images of acceptable quality for remote sensing tasks. The results are illustrated in Table I. Compared with UniControl on the CNSATMAP dataset, which is also designed for remote sensing image generation [66], [67], our strategy achieves consistently better KID performance, as evidenced by the lower KID score reported in Table I.

C. Evaluation of Model Performance

This study evaluates the performance of various models, including FlashInternImage, Vision Transformer, and DViT, through metrics such as overall accuracy (OA), mean accuracy (mAcc), Kappa coefficient, precision (macro), recall (macro), and F1-score (macro). These metrics provide comprehensive insights into model effectiveness for land-cover classification tasks.

Overall accuracy quantifies the proportion of correctly classified instances across all classes and is computed as

$$OA = \frac{TP + TN}{TP + TN + FP + FN} \quad (1)$$

where TP, TN, FP, and FN represent true positives, true negatives, false positives, and false negatives, respectively.

Mean accuracy reflects the average classification accuracy across different classes, highlighting the balanced performance of models, especially in datasets with class imbalance [68]. The mAcc is computed as

$$mAcc = \frac{1}{N} \sum_{i=1}^N \frac{TP_i}{TP_i + FN_i} \quad (2)$$

where N is the total number of classes.

The Cohen’s Kappa coefficient provides an evaluation of the model’s performance by considering agreement occurring by chance [68]. It is calculated as

$$\kappa = \frac{P_o - P_e}{1 - P_e} \quad (3)$$

where P_o denotes the observed agreement and P_e represents the probability of random agreement.

Precision (macro) is calculated as the mean of class-wise precision, capturing the model’s accuracy in predicting each class correctly and reducing the impact of false positives [69]:

$$\text{Precision}_{\text{macro}} = \frac{1}{N} \sum_{i=1}^N \frac{TP_i}{TP_i + FP_i}. \quad (4)$$

Recall (macro), representing the average recall across all classes, indicates the model’s capability to identify all relevant instances per class, thereby accounting for false negatives:

$$\text{Recall}_{\text{macro}} = \frac{1}{N} \sum_{i=1}^N \frac{TP_i}{TP_i + FN_i}. \quad (5)$$

The F1-score (macro) harmonizes precision and recall into a single performance metric, providing a balanced measure that is particularly beneficial when precision and recall are equally critical [69]:

$$F1_{\text{macro}} = \frac{1}{N} \sum_{i=1}^N \frac{2 \times \text{Precision}_i \times \text{Recall}_i}{\text{Precision}_i + \text{Recall}_i}. \quad (6)$$

These metrics collectively provide an in-depth evaluation, enabling a nuanced understanding of each model’s strengths and areas requiring improvement for effective land-cover classification.

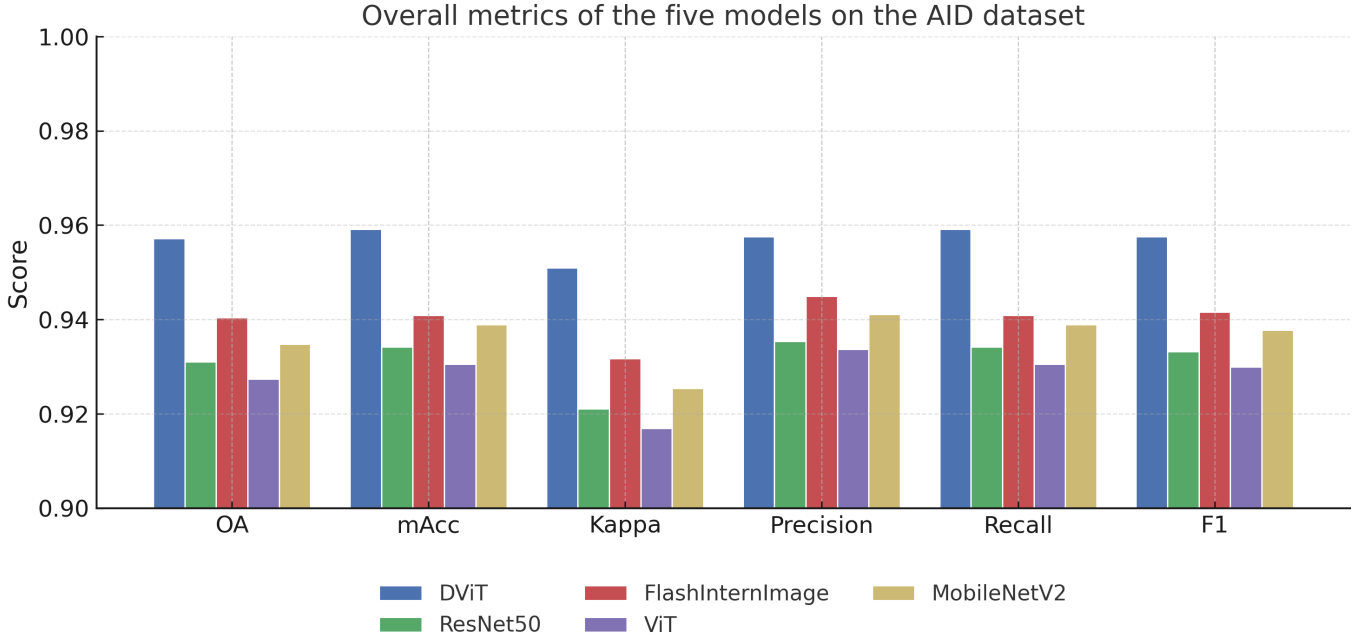


Fig. 3. Overall metrics of the five models on the AID dataset. The evaluation metrics include Overall Accuracy (OA), mAcc, Kappa Coefficient (Kappa), Precision, Recall and F1 Score (F1).

1) *Hyperparameter Setup*: In this study, all models, including MobileNetV2, Resnet50, Vision Transformer (ViT), FlashInternImage, and Deformable Vision Transformer (DViT), were trained for 30 epochs using a batch size of 16 and a learning rate initialized at 1×10^{-4} . The AdamW optimizer [70] was employed to optimize the model parameters, providing improved weight-decay handling and convergence stability during training. The input images were uniformly resized to a resolution of 512×512 pixels and normalized using mean and standard deviation values of mean = [0.485, 0.456, 0.406] and std = [0.229, 0.224, 0.225], respectively.

Network training was conducted by minimizing the cross-entropy loss function, defined as

$$\mathcal{L}_{CE} = -\frac{1}{N} \sum_{i=1}^N \sum_{c=1}^C y_{ic} \log(\hat{y}_{ic}) \quad (7)$$

where N is the number of training samples in each batch, C denotes the total number of classes, y_{ic} represents the ground-truth indicator (with a value of 1 if sample i belongs to class c and 0 otherwise), and \hat{y}_{ic} is the predicted probability of sample i belonging to class c .

Additionally, the proposed DViT model is configured using the following configurations. The DCNv4 backbone uses a base width of 80 channels with four stages of channel dimensions [80, 160, 320, 640] and depths [3, 4, 16, 6]. The offset scale is set to 1.0 and the maximum DropPath rate in the backbone is 0.20. On top of the backbone, the Transformer encoder operates with an embedding dimension of 384, a depth of 7 layers, 8 attention heads, head dimension of 48, and an MLP dimension of 1536. The attention dropout and embedding dropout are both set to 0.1, and the maximum DropPath rate in the Transformer is 0.15.

2) *Results Analysis*: Figure 3 summarizes the overall performance of the five backbones (ViT, FlashInternImage, ResNet50, MobileNetV2, and DViT) across six metrics: OA, mAcc, Cohen’s Kappa, macro Precision, macro Recall, and macro F1-score. DViT clearly dominates all competitors, reaching an OA of 0.9572 and mAcc of 0.9592, which correspond to gains of 1.68 and 1.83 percentage points over the second-best model (FlashInternImage), and more than 2 percentage points over the vanilla ViT baseline. Similarly, DViT attains the highest Kappa value (0.9510), indicating the strongest agreement with ground-truth labels after correcting for chance, and achieves the best macro Precision, Recall, and F1-score (0.9576, 0.9592, and 0.9576, respectively). ResNet50 and MobileNetV2 form a middle tier, consistently outperforming ViT but falling short of DViT and FlashInternImage, while ViT lags behind in all metrics despite serving as the Transformer baseline. Overall, the bar plot highlights that DViT delivers the most balanced and robust performance across all global metrics without increasing model capacity.

Table II provides a detailed per-class view over the eight AID categories (Beach, Bridge, Desert, Forest, Mountain, Pond, Port, and River). DViT achieves perfect or near-perfect performance for Desert, Forest, and Pond (accuracy ≥ 0.9870 and F1-score ≥ 0.9709), and delivers the highest F1-score for four hydrology-related categories: Bridge (0.9457), Pond (0.9870), Port (0.9624), and River (0.9459). These classes are precisely those with elongated, deformation-rich geometries where deformable attention is expected to be most beneficial. FlashInternImage and MobileNetV2 show strong results on Mountain, Port, and Forest, while ViT yields the best Beach accuracy and F1-score but degrades noticeably on Bridge, Pond, and River. ResNet50 performs competitively

TABLE II
PER-CLASS METRICS (ACCURACY, PRECISION, F1-SCORE, AND KAPPA) OF THE FIVE MODELS ON THE AID DATASET.

Class	Model	Accuracy	Precision	F1-score	Kappa
Beach	DViT (Ours)	0.9306	0.9710	0.9504	0.9429
	ResNet50	0.9167	0.9706	0.9429	0.9343
	FlashInternImage	0.9306	0.9853	0.9571	0.9507
	ViT	0.9861	0.9595	0.9726	0.9683
	MobileNetV2	0.9444	0.9714	0.9577	0.9513
Bridge	DViT (Ours)	0.9242	0.9683	0.9457	0.9383
	ResNet50	0.9091	0.7692	0.8333	0.8077
	FlashInternImage	0.8182	0.9474	0.8780	0.8624
	ViT	0.9394	0.7848	0.8552	0.8328
	MobileNetV2	0.9545	0.8400	0.8936	0.8766
Desert	DViT (Ours)	1.0000	0.9524	0.9756	0.9725
	ResNet50	1.0000	0.9375	0.9677	0.9635
	FlashInternImage	0.9833	0.9672	0.9752	0.9721
	ViT	1.0000	1.0000	1.0000	1.0000
	MobileNetV2	0.9833	0.9833	0.9833	0.9812
Forest	DViT (Ours)	1.0000	0.9434	0.9709	0.9678
	ResNet50	0.9800	0.9608	0.9703	0.9672
	FlashInternImage	0.9600	0.9796	0.9697	0.9666
	ViT	0.9400	0.9592	0.9495	0.9444
	MobileNetV2	0.9800	0.9800	0.9800	0.9779
Mountain	DViT (Ours)	0.9706	0.8800	0.9231	0.9113
	ResNet50	0.9706	0.9565	0.9635	0.9582
	FlashInternImage	0.9853	0.8933	0.9371	0.9274
	ViT	0.9706	0.8684	0.9167	0.9038
	MobileNetV2	0.9853	0.8272	0.8993	0.8833
Pond	DViT (Ours)	0.9870	0.9870	0.9870	0.9848
	ResNet50	0.9221	0.9467	0.9342	0.9234
	FlashInternImage	0.9610	1.0000	0.9801	0.9769
	ViT	0.8571	0.9429	0.8980	0.8818
	MobileNetV2	0.8571	0.9851	0.9167	0.9038
Port	DViT (Ours)	0.9275	1.0000	0.9624	0.9571
	ResNet50	0.8551	0.9833	0.9147	0.9032
	FlashInternImage	0.9420	0.9420	0.9420	0.9335
	ViT	0.8986	1.0000	0.9466	0.9392
	MobileNetV2	0.9130	0.9844	0.9474	0.9399
River	DViT (Ours)	0.9333	0.9589	0.9459	0.9373
	ResNet50	0.9200	0.9583	0.9388	0.9291
	FlashInternImage	0.9467	0.8452	0.8931	0.8746
	ViT	0.8533	0.9552	0.9014	0.8864
	MobileNetV2	0.8933	0.9571	0.9241	0.9123

on Mountain and Forest but is generally weaker on Bridge and Pond. Taken together, the per-class statistics confirm that DViT provides the most consistent and reliable performance across all eight categories, especially on geometrically complex hydrological classes, whereas the other backbones tend to specialize in a subset of scenes or exhibit larger per-class variation.

Figure 4 presents the normalized confusion matrices for all five backbones (ViT, FlashInternImage, ResNet50, MobileNetV2, and DViT), highlighting their per-class recognition behavior across the eight AID categories. Overall, all models classify Desert, Forest, and Mountain almost perfectly, whereas most errors are concentrated in the hydrology-related classes Bridge, Pond, Port, and River. Among the five backbones, DViT exhibits the sharpest diagonal and the most uniform performance, with recalls above 0.92 for all classes and near-perfect recognition of Desert, Forest, and Pond. ResNet50 and MobileNetV2 also achieve strong diagonals for most categories but still show noticeably higher confusion between

Bridge, Port, and River than DViT. FlashInternImage attains high recall on Mountain, Pond, and River, yet misclassifies a non-trivial portion of river scenes as bridges. ViT, in contrast, delivers the best recall on Beach but suffers more from misclassification in Pond, Port, and River. Taken together, these matrices confirm that DViT provides the cleanest and most balanced confusion pattern across all eight classes, especially for geometrically complex hydrological categories, while the other backbones either specialize in a subset of classes or exhibit larger off-diagonal error rates.

D. Ablation Studies

To quantify the contribution of each component in the proposed LC4-DViT pipeline, we conduct ablation experiments on the DViT model by selectively enabling Real-ESRGAN-based super-resolution (SupreR) and diffusion-based data augmentation (Diffusion), as summarized in Table III. Starting from a baseline DViT trained on the original AID images without SupreR or Diffusion, the model achieves an OA of

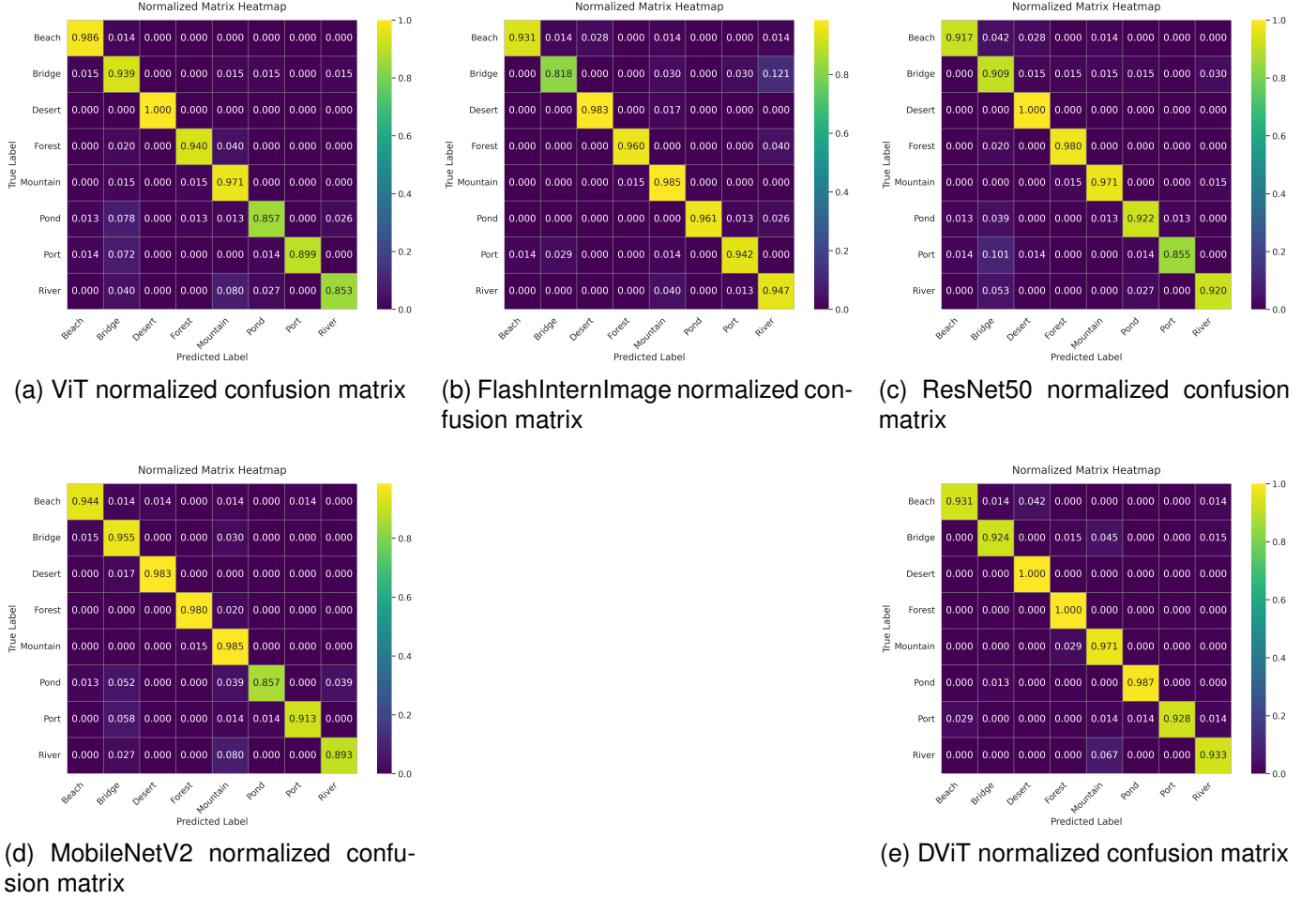


Fig. 4. Normalized confusion matrices of the Five models.

TABLE III
ABLATION EXPERIMENTS RESULTS.

Model	SupreR	Diffusion	Overall Accuracy	Mean Accuracy	Cohen-Kappa	Precision (macro)	Recall (macro)	F1-score (macro)
DViT	✓	✓	0.9162	0.9185	0.9041	0.9213	0.9185	0.9183
			0.9311	0.9341	0.9211	0.9326	0.9341	0.9326
	✓	✓	0.9367	0.9383	0.9275	0.9386	0.9383	0.9380
			0.9572	0.9592	0.9510	0.9576	0.9592	0.9576

0.9162, mAcc of 0.9185, and Kappa of 0.9041. Introducing only SupreR improves OA to 0.9311 (+1.49 percentage points) and Kappa to 0.9211, indicating that enhancing the spatial detail of the inputs benefits both overall and per-class recognition. When only Diffusion is enabled, OA further increases to 0.9367 and Kappa to 0.9275, demonstrating that class-balanced, description-driven synthetic samples bring a larger gain than super-resolution alone by enriching geometric and appearance variability in the training set.

The full LC4-DViT configuration, which combines SupreR and Diffusion, yields the best performance across all metrics, reaching an OA of 0.9572, mAcc of 0.9592, Kappa of 0.9510, and a macro F1-score of 0.9576. Compared with the baseline DViT, this corresponds to absolute improvements of 4.10, 4.07, and 4.69 percentage points in OA, mAcc, and Kappa,

respectively, and a 3.93 percentage point gain in macro F1. These results indicate that super-resolution and diffusion-based augmentation are complementary: super-resolution provides cleaner, higher-frequency details, while diffusion-based sample creation increases class balance and deformation diversity. Their combination leads to a substantially more robust DViT classifier for land-cover mapping than either component in isolation.

E. Evaluation of Model Attention via Heatmaps

To gain deeper insight into the regions influencing the classification decisions of the models, heatmaps were generated to illustrate spatial attention on input images. Specifically, class activation mapping (CAM) and Gradient-weighted Class Activation Mapping (Grad-CAM) techniques were employed

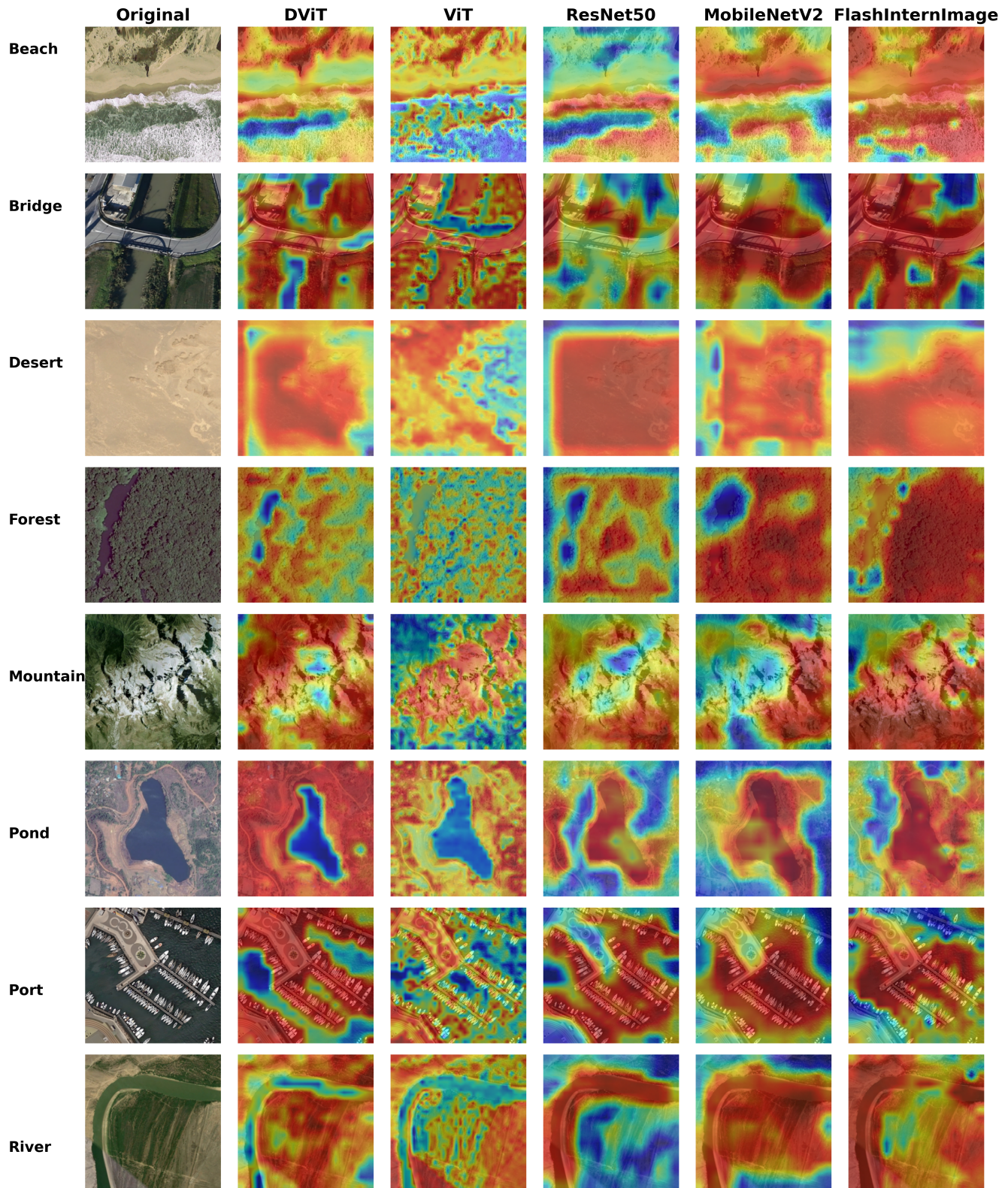


Fig. 5. Model's attention to key areas of the images. compares class-activation heatmaps of different models for eight scene categories (Beach, Bridge, Desert, Forest, Mountain, Pond, Port, and River). The first column is the original scene and the other columns are the attention heatmaps of different models.

[71]. A hook is registered at the final convolutional layer to collect gradients, which are then applied to the layer output to produce activation maps. These activation maps are subsequently weighted to highlight regions significantly influencing classification decisions, enabling clear visualization of the models’ decision rationale.

In Fig. 5, we present class-activation heatmaps for eight representative categories (Beach, Bridge, Desert, Forest, Mountain, Pond, Port, and River) generated by our DViT and four competing backbones (ViT, ResNet50, MobileNetV2, and FlashInternImage). Across all categories, the networks generally focus on semantically meaningful regions—such as shoreline and surf zones in Beach scenes, bridge decks in Bridge images, sandy textures in Desert, dense canopy in Forest, mountain ridges in Mountain, water bodies and boundaries in Pond and River, and dock structures in Port—indicating that they have learned category-relevant spatial cues. Nevertheless, DViT produces noticeably more compact and boundary-consistent responses than the baselines. For water-related classes (Beach, Pond, River), the high-activation areas of DViT tightly follow water-land interfaces, whereas ViT and especially the CNN-based ResNet50 and MobileNetV2 show more diffused attention over surrounding homogeneous regions. In Bridge, Port, and Mountain scenes, DViT concentrates on slender man-made structures and ridge patterns, while the other models frequently spread activation to irrelevant roads or background terrain. Compared with FlashInternImage, DViT also yields less noisy and more spatially coherent heatmaps. These qualitative results demonstrate that the proposed DViT captures long-range dependencies while preserving fine-grained structural details, leading to more accurate localization of class-discriminative regions in high-resolution remote sensing images.

Based on the eight representative heatmaps, we further used them for an LLM-based (GPT-4o) evaluation of heatmap quality. For each image-model pair, GPT-4o was prompted as an impartial judge of remote-sensing attention maps with the following structure:

- **Inputs.** The ground-truth scene category, the original RGB image, and the corresponding attention heatmap, where warmer colors indicate higher attention.
- **Evaluation focus.** Assess only the spatial alignment between high-activation regions and the semantic regions of the ground-truth class (e.g., water body, shoreline, river course, forest canopy, mountain ridge, bridge span), ignoring model architecture, training details, and any numerical scores.
- **Scoring rubric.** Assign an integer score $s \in \{0, 1, 2, 3\}$:
 - $s = 0$: attention almost entirely on irrelevant areas, with class-relevant regions largely ignored;
 - $s = 1$: partial overlap with relevant regions, but a substantial portion of strong attention on irrelevant areas;
 - $s = 2$: most strong attention on key class regions and structures, with limited spillover to background;
 - $s = 3$: near-perfect alignment with class-discriminative regions and boundaries, with minimal unnecessary

TABLE IV
AVERAGE GPT4O-JUDGE SCORES (0–3 SCALE) OVER EIGHT SAMPLED CATEGORIES.

Model	DViT	FlashInternImage	ViT	ResNet50	MobileNetV2
Average Score	2.625	2.5	2.25	2.0	2.5

TABLE V
PER-CLASS METRICS ON THE THREE-CLASS SIRI-WHU SUBSET.

Class	Model	Accuracy	Precision	F1-score	Kappa
Harbor	DViT (Ours)	1.0000	0.8696	0.9302	0.8916
	ResNet50	0.9500	0.8636	0.9048	0.8537
	FlashInternImage	0.8500	0.7727	0.8095	0.7073
	ViT	0.8500	0.8947	0.8718	0.8101
	MobileNetV2	0.8500	0.9444	0.8947	0.8462
Pond	DViT (Ours)	1.0000	0.9524	0.9756	0.9630
	ResNet50	0.9500	0.8261	0.8837	0.8193
	FlashInternImage	1.0000	0.8696	0.9302	0.8916
	ViT	0.8500	0.8947	0.8718	0.8101
	MobileNetV2	1.0000	0.8000	0.8889	0.8235
River	DViT (Ours)	0.8000	1.0000	0.8889	0.8421
	ResNet50	0.7000	0.9333	0.8000	0.7200
	FlashInternImage	0.7500	1.0000	0.8571	0.8000
	ViT	0.8500	0.7727	0.8095	0.7073
	MobileNetV2	0.8000	0.9412	0.8649	0.8052

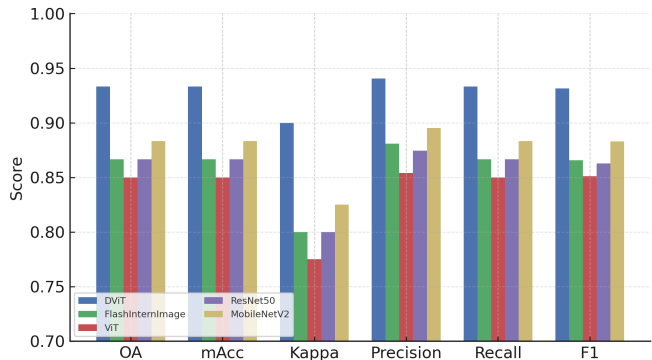


Fig. 6. Overall metrics (OA, mAcc, Kappa, macro Precision, macro Recall, macro F1-score) of the five models on the three-class SIRI-WHU subset (Harbor, Pond, River).

focus.

- **Outputs.** A single discrete score and a brief natural-language explanation supporting the rating.

Table IV reports the average LLM-Judge scores across the eight categories. DViT attains the highest mean score (2.625), indicating the most consistent alignment between its high-activation regions and class-discriminative landform features. FlashIntern and MobileNetV2 obtain identical intermediate scores (2.5), while ViT performs slightly worse (2.25). ResNet50 achieves the lowest average score (2.0), reflecting more diffuse or misplaced attention. These results are consistent with our qualitative observations and further support the superior spatial interpretability of DViT.

F. Cross-dataset Evaluation on SIRI-WHU

To further validate the generalization ability of the proposed LC4-DViT framework, we conduct additional experiments on

a three-class subset (Harbor, Pond, River) of the SIRI-WHU dataset. Figure 6 summarizes six overall metrics—overall accuracy (OA), mean accuracy (mAcc), Cohen’s Kappa, macro precision, macro recall, and macro F1-score—for all five models. DViT achieves the best performance across all indicators, reaching an OA and mAcc of 0.9333, Kappa of 0.9000, macro precision of 0.9406, macro recall of 0.9333, and macro F1-score of 0.9316. Compared with the strongest CNN baseline (MobileNetV2), this corresponds to gains of 5.0 percentage points in OA and mAcc, 7.5 percentage points in Kappa, and around 4–5 percentage points in the macro precision and F1-score, confirming that the deformation-aware transformer backbone transfers well to a different sensor and geographic distribution.

Table V reports per-class metrics for Harbor, Pond, and River. DViT attains perfect accuracy on both Harbor and Pond (1.0000) with high F1-scores (0.9302 and 0.9756, respectively) and the highest Kappa values among all models, indicating both strong correctness and robust agreement beyond chance. On the more challenging River class, DViT obtains the highest precision (1.0000) and the best Kappa (0.8421), while maintaining competitive accuracy and F1-score. These results demonstrate that the proposed DViT not only improves overall performance on SIRI-WHU but also provides consistent gains on hydrology- and infrastructure-related classes, supporting its effectiveness for cross-dataset land-cover classification.

IV. DISCUSSION

Across ten independent runs, coupling class-balanced, description-driven diffusion sampling with a deformation-aware Vision Transformer (DViT) yields consistent gains on the selected AID subset. As summarized in Fig. 3, the proposed LC4-DViT achieves 0.9572 overall accuracy, 0.9592 mean class accuracy, 0.9510 Cohen’s Kappa, and 0.9576 macro-averaged F1-score, outperforming the strongest CNN baseline (FlashInternImage) by 1.68, 1.83, 1.93, and 1.60 percentage points, respectively. Relative to the vanilla ViT, the gains are even larger, with improvements of 2.98 percentage points in overall accuracy, 2.86 in mean accuracy, 3.41 in Kappa, and 2.76 in macro F1. These aggregate metrics indicate that LC4-DViT consistently improves both global and class-balanced performance without increasing model capacity.

The per-class results in Table II provide a more granular view of these trends. We deliberately focus on eight AID classes—Beach, Bridge, Desert, Forest, Mountain, Pond, Port, and River—because they cover a compact but challenging spectrum of hydrology- and infrastructure-related land covers embedded in diverse surroundings. Beach, Pond, Port, and River directly represent surface water or water-land interfaces, while Bridge links built infrastructure with hydrological corridors. Desert, Forest, and Mountain serve as confounding context classes, introducing highly variable textures and topographies that make the hydrological categories harder to separate. This design yields a stress test in which misclassifications are both common and practically costly, for example when confusing small rivers with ports or misidentifying narrow bridges embedded in dense urban fabric.

Under this setting, DViT achieves the highest F1-score among all five backbones for four of the most critical water/infrastructure classes—Bridge (0.9457), Pond (0.9870), Port (0.9624), and River (0.9459)—while remaining competitive on Beach, Desert, Forest, and Mountain. In contrast, ViT attains the best F1-score only on Beach and Desert, and MobileNetV2 or ResNet50 dominate primarily on the contextual class Forest and the topographically complex class Mountain. These patterns suggest that deformable feature extraction is particularly advantageous when the target occupies a small fraction of the scene and exhibits elongated or curvilinear geometries, whereas standard CNNs and ViTs can still suffice for large, relatively homogeneous regions.

To further test cross-dataset robustness and reduce the risk of overfitting to Google Earth imagery, we evaluate the same set of backbones on three hydrology-related classes from SIRI-WHU (Harbor, Pond, River). Averaged over these classes, DViT achieves the best overall accuracy (0.9333), F1-score (0.9316), and Kappa (0.8989), improving upon the strongest baseline (MobileNetV2) by approximately 5.0, 4.9, and 7.4 percentage points, respectively. Per-class metrics show that DViT attains the highest F1-score on all three SIRI-WHU classes (0.9302 for Harbor, 0.9756 for Pond, and 0.8889 for River), confirming that the gains observed on AID transfer to independent data acquired with different imaging characteristics and labeling protocols.

Ablation experiments further disentangle the contributions of the generative and architectural components. When the deformable backbone is replaced by a standard ViT while retaining the diffusion-based augmentation, performance drops across all overall metrics; conversely, enabling DCNv4 but training only on the original imbalanced dataset also yields weaker results than the full LC4-DViT pipeline. The combination of Stable Diffusion-based sample creation and Real-ESRGAN super-resolution gives the largest improvement, especially for minority hydrological classes, indicating that both the diversity and the geometric fidelity of the synthetic images are important. Removing the super-resolution stage leads to blurrier synthetic boundaries and noticeably lower scores on Bridge and River, while omitting diffusion-based augmentation mainly harms performance on underrepresented categories such as Port and Pond.

Beyond accuracy, interpretability is critical for deploying geospatial AI in environmental monitoring. Qualitative Grad-CAM visualizations show that DViT more sharply localizes hydrological structures—such as bridge decks, harbor basins, and narrow river channels—than the baselines, whose attention often spills into surrounding urban or vegetated areas. To make this assessment more systematic and less subjective, we introduce an LLM-based judge that leverages GPT-4o to evaluate anonymized attention heatmaps. For each test image and class, GPT-4o receives the original image, the ground-truth label, and superposed heatmaps from all backbones, and is prompted to score which heatmap best highlights class-defining regions. Across both AID and WHU-SIRI, DViT receives the highest average rating, aligning the quantitative accuracy improvements with an external assessment of interpretability and providing additional evidence that its

deformation-aware attention is better matched to geospatial semantics.

Two limitations remain particularly salient. First, all experiments use RGB imagery; the absence of near- and shortwave-infrared bands limits separability at water-vegetation and water-urban boundaries, where spectral differences could provide stronger cues than texture alone. Extending DViT to multispectral or hyperspectral inputs is straightforward (e.g., by adapting the patch embedding to higher channel counts) and is expected to further stabilize performance on mixed pixels. Second, while our diffusion pipeline is carefully gated using Kernel Inception Distance (KID), a residual synthetic-real gap persists, especially for texture-dominated scenes such as sandy beaches. Tightening geometric and texture constraints in the diffusion model, and fine-tuning it on in-domain aerial imagery, should reduce this gap and may yield additional gains. Finally, although the SIRI-WHU experiments provide encouraging cross-dataset evidence, broader validation on raw sensor data (e.g., Sentinel-2, Gaofen) and under explicit domain-adaptation settings remains an important direction for future work.

V. CONCLUSIONS

This study proposes LC4-DViT, an end-to-end framework that jointly addresses two key bottlenecks in remote-sensing land-cover classification: data scarcity/imbalance and the difficulty of modeling irregular, deformation-rich landforms. On the data side, we design a GPT-4o-guided, Stable Diffusion-based augmentation pipeline with Real-ESRGAN super-resolution that generates class-balanced, high-fidelity samples tailored to hydrology- and infrastructure-related categories. On the model side, we introduce DViT, which fuses a DCNv4 deformable backbone with a Vision Transformer encoder to capture both local geometric detail and global scene context.

Comprehensive experiments on eight AID classes (Beach, Bridge, Desert, Forest, Mountain, Pond, Port, River) and three SIRI-WHU classes (Harbor, Pond, River) demonstrate that this combination is effective. On AID, LC4-DViT achieves 0.9572 overall accuracy, 0.9592 mean accuracy, 0.9510 Kappa, and 0.9576 macro F1-score, outperforming strong CNN (ResNet50, MobileNetV2, FlashInternImage) and Transformer (ViT) baselines while using a comparable number of parameters. Per-class analysis shows that DViT is particularly advantageous for hydrology- and infrastructure-related categories, yielding the highest F1-scores for Bridge, Pond, Port, and River and substantially reducing confusion among these visually similar classes. Cross-dataset experiments on WHU-SIRI confirm that these gains are not confined to a single benchmark: DViT attains the best average overall accuracy, F1-score, and Kappa across Harbor, Pond, and River, highlighting its robustness to changes in imaging conditions and labeling schemes. Ablation studies verify that both components of LC4-DViT are necessary: removing the diffusion-based land-cover creation pipeline or the super-resolution stage significantly degrades performance, as does replacing the deformable backbone with a standard ViT. Finally, by integrating Grad-CAM

with an LLM-based judge powered by GPT-4o, we show that DViT not only achieves higher numerical accuracy but also produces attention maps that external evaluators deem most consistent with class-defining landform structures.

Taken together, these findings indicate that combining description-driven generative augmentation with deformation-aware transformers is a promising direction for high-resolution land-cover mapping. The proposed LC4-DViT framework provides a practical, extensible tool for improving the recognition of hydrological and infrastructure classes that are central to flood-risk assessment, blue-green infrastructure planning, and broader environmental monitoring. Future work will extend this approach to multispectral and hyperspectral sensors, larger class vocabularies, and additional geographic regions, as well as exploring tighter integration between diffusion models, deformable attention, and LLM-based evaluators for fully closed-loop geospatial AI systems.

DATA AVAILABILITY

The original AID dataset is publicly available at <https://captain-whu.github.io/AID/>. And the SIRI-WHU dataset is publicly available at <https://opendatalab.com/OpenDataLab/SIRI-WHU/tree/main>.

CONFLICT OF INTEREST

The authors declare that they have no conflict of interest.

REFERENCES

- [1] K. D. Musetsho, M. Chitakira, and A. Ramoelo, "Ecosystem service valuation for a critical biodiversity area: Case of the Mphaphuli community, South Africa," *Land*, vol. 11, p. 1696, 2022.
- [2] H. Chen and W. Cai, "Multi-scale analysis of water purification ecosystem service flow in Taihu basin for land management and ecological compensation," *Land*, vol. 13, p. 1694, 2024.
- [3] C. Li, H. Cui, and X. Tian, "Remote sensing image segmentation of wetlands in Macau based on machine learning," in *Proc. Int. Conf. Big Data, Information and Intelligent Engineering*, 2023.
- [4] W. Zhou, T. Wu, and X. Tao, "Exploring the spatial and seasonal heterogeneity of the cooling effect of an urban river on a landscape scale," *Sci. Rep.*, vol. 14, p. 8327, 2024.
- [5] B. S. Allain, C. Marechal, and C. Pottier, "Wetland water segmentation using multi-angle and polarimetric RADARSAT-2 datasets," in *Proc. IEEE Int. Geosci. Remote Sens. Symp. (IGARSS)*, 2012, pp. 4915–4917.
- [6] Z. Y. Ke, A. Ru, and X. J. Li, "ANN based high spatial resolution remote sensing wetland classification," in *Proc. 14th Int. Symp. Distributed Computing and Applications for Business Engineering and Science (DCABES)*, 2015, pp. 180–183.
- [7] Y. Gui, W. Li, X. G. Xia, R. Tao, and A. Yue, "Infrared attention network for woodland segmentation using multispectral satellite images," *IEEE Trans. Geosci. Remote Sens.*, vol. 60, p. 5627214, 2022.
- [8] H. Cui, J. Liang, C. Li, and X. Tian, "Improved convolutional neural network with attention mechanisms for river extraction," *Water*, vol. 17, no. 12, p. 1762, 2025.
- [9] M. J. Mashala, T. Dube, B. T. Mudereri, K. K. Ayisi, and M. R. Ramudzuli, "A systematic review on advancements in remote sensing for assessing and monitoring land-use and land-cover changes impacts on surface water resources in semi-arid tropical environments," *Remote Sens.*, vol. 15, p. 3926, 2023.
- [10] C. Li, H. Cui, and X. Tian, "A novel CA-RegNet model for Macau wetlands auto segmentation based on GF-2 remote sensing images," *Appl. Sci.*, vol. 13, p. 12178, 2023.
- [11] M. Lupa, A. Pelka, M. Mlynarczuk, J. Staszal, and K. Adamek, "Why rivers disappear—remote sensing analysis of post-mining factors using the example of the Sztola River, Poland," *Remote Sens.*, vol. 16, p. 111, 2024.

- [12] J. Ho, A. Jain, and P. Abbeel, "Denoising diffusion probabilistic models," in *Advances in Neural Information Processing Systems*, vol. 33, 2020, pp. 6840–6851.
- [13] Y. Song, J. Sohl-Dickstein, D. P. Kingma, A. Kumar, S. Ermon, and B. Poole, "Score-based generative modeling through stochastic differential equations," *arXiv:2011.13456*, 2020.
- [14] C. Li, K. Zhou, T. Liu *et al.*, "AVD2: Accident video diffusion for accident video description," *arXiv:2502.14801*, 2025.
- [15] T. Xu, P. Zhang, Q. Huang *et al.*, "AttnGAN: Fine-grained text-to-image generation with attentional GANs," in *Proc. IEEE/CVF Conf. Comput. Vis. Pattern Recognit. (CVPR)*, 2018, pp. 1316–1324.
- [16] S. Ruan, Y. Zhang, K. Zhang *et al.*, "DAE-GAN: Dynamic aspect-aware GAN for text-to-image synthesis," in *Proc. IEEE/CVF Conf. Comput. Vis. Pattern Recognit. (CVPR)*, 2021, pp. 13960–13969.
- [17] R. Zhao and Z. Shi, "Text-to-remote-sensing-image generation with structured generative adversarial networks," *IEEE Geosci. Remote Sens. Lett.*, vol. 19, pp. 1–5, 2021.
- [18] M. Tao, H. Tang, F. Wu *et al.*, "DF-GAN: A simple and effective baseline for text-to-image synthesis," in *Proc. IEEE/CVF Conf. Comput. Vis. Pattern Recognit. (CVPR)*, 2022, pp. 16515–16525.
- [19] Y. Zhou, R. Zhang, C. Chen *et al.*, "Towards language-free training for text-to-image generation," in *Proc. IEEE/CVF Conf. Comput. Vis. Pattern Recognit. (CVPR)*, 2022, pp. 17907–17917.
- [20] A. Nichol, P. Dhariwal, A. Ramesh *et al.*, "GLIDE: Towards photorealistic image generation and editing with text-guided diffusion models," *arXiv:2112.10741*, 2021.
- [21] Saharia, C., Chan, W., Saxena, S., Li, L., Whang, J., Denton, E. L., Ghasemipour, K., Gontijo Lopes, R., Karagol Ayan, B., Salimans, T., *et al.* Photorealistic text-to-image diffusion models with deep language understanding. *Advances in Neural Information Processing Systems*, **35**, 36479–36494 (2022).
- [22] A. Sebaq and M. ElHelw, "RSDiff: Remote-sensing image generation from text using diffusion model," *arXiv:2309.02455*, 2023.
- [23] O. Baghirli, H. Askarov, I. Ibrahimli, I. Bakhishov, and N. Nabiyeu, "SatDM: Synthesizing realistic satellite images with semantic-layout conditioning using diffusion models," *arXiv:2309.16812*, 2023.
- [24] S. Khanna, P. Liu, L. Zhou *et al.*, "DiffusionSat: A generative foundation model for satellite imagery," *arXiv:2312.03606*, 2023.
- [25] D. Tang, X. Cao, X. Hou, Z. Jiang, J. Liu, and D. Meng, "CRS-Diff: Controllable remote sensing image generation with diffusion model," *IEEE Trans. Geosci. Remote Sens.*, pp. 1–14, 2024.
- [26] M. De Vita and V. Belagiannis, "Diffusion model guided sampling with pixel-wise aleatoric uncertainty estimation," *arXiv:2412.00205*, 2024.
- [27] N. Li, J. Zhang, and J. Cui, "Have we unified image generation and understanding yet? An empirical study of GPT-4o's image generation ability," *arXiv:2504.08003*, 2025.
- [28] A. Tzepkenlis, K. Marthoglou, and N. Grammalidis, "Efficient deep semantic segmentation for land cover classification using Sentinel imagery," *Remote Sens.*, vol. 15, p. 2027, 2023.
- [29] D. Marmanis, M. Datcu, T. Esch, and U. Stilla, "Deep learning Earth observation classification using ImageNet pre-trained networks," *IEEE Geosci. Remote Sens. Lett.*, vol. 13, no. 1, pp. 105–109, 2016.
- [30] C. Li, S. Chen, Y. Ma, M. Song, X. Tian, and H. Cui, "Wheat pest identification based on deep learning techniques," in *Proc. IEEE 7th Int. Conf. Big Data and Artificial Intelligence (BDAl)*, 2024, pp. 87–91.
- [31] C. Li, Y. Tian, X. Tian, Y. Zhai, H. Cui, and M. Song, "An advancing GCT-Inception-ResNet-V3 model for arboreal pest identification," *Agronomy*, vol. 14, p. 864, 2024.
- [32] G. S. Xia, J. Hu, F. Hu *et al.*, "AID: A benchmark dataset for performance evaluation of aerial scene classification," *IEEE Trans. Geosci. Remote Sens.*, vol. 55, no. 7, pp. 3965–3981, 2017.
- [33] Y. Ma, Y. Huang, C. Li *et al.*, "A hybrid brain-computer interface based wearable exoskeleton system for fine-grained hand rehabilitation," in *Proc. IEEE BioCAS*, 2024.
- [34] S. Chen, C. Li, Y. Ma *et al.*, "Deep learning techniques for lunar impact crater identification based on CCD and DEM data," in *Image Processing, Computer Vision, and Pattern Recognition and Information and Knowledge Engineering*, CSCE 2024, 2025.
- [35] A. Vali, S. Comai, and M. Matteucci, "Deep learning for large-scale image classification of high-resolution aerial imagery," *Appl. Artif. Intell.*, vol. 34, no. 14, pp. 1177–1196, 2020.
- [36] S. Khan, M. Khan, A. Rauf *et al.*, "Remote sensing image classification: A comprehensive review and possible future directions," *Artif. Intell. Rev.*, 2022.
- [37] X. X. Zhu *et al.*, "A survey of remote sensing image classification based on CNNs," *Geo-spatial Inf. Sci.*, vol. 26, no. 1, pp. 67–95, 2019.
- [38] K. Wang, S. Lu, and S. Jiang, "Unseen obstacle detection via monocular camera against speed change and background noise," in *Proc. HCII*, 2023.
- [39] M. Khan, A. Hanan, M. Gazzea *et al.*, "Transformer-based land use and land cover classification with explainability using satellite imagery," *Sci. Rep.*, vol. 14, p. 16744, 2024.
- [40] P. Xiao, F. Sun, K. Wang *et al.*, "Positioning performance analysis of real-time BDS-3 PPP B2b/INS tightly coupled integration in urban environments," *Adv. Space Res.*, vol. 72, no. 9, pp. 4008–4020, 2023.
- [41] S. Han, M. Zhao, K. Wang, J. Dong, and A. Su, "Cross-modal image matching based enhancement to MEMS INS for UAV navigation in GNSS denied environments," *Appl. Sci.*, vol. 13, no. 14, p. 8238, 2023.
- [42] L. Zhao, J. Zhang *et al.*, "RoadFormer: Pyramidal deformable vision transformers for road network extraction with remote sensing images," *ISPRS J. Photogramm. Remote Sens.*, 2022.
- [43] R. Naushad and T. Kaur, "Deep transfer learning for land use and land cover classification: A comparative study," *Sensors*, vol. 21, p. 8083, 2021.
- [44] N. Alosaimi, H. Alhichri, Y. Bazi *et al.*, "Self-supervised learning for remote sensing scene classification under the few-shot scenario," *Sci. Rep.*, vol. 13, p. 433, 2023.
- [45] L. Scheibenreif, J. Hanna, M. Mommert, and D. Borth, "Self-supervised vision transformers for land-cover segmentation and classification," in *Proc. CVPR EarthVision Workshop*, 2022.
- [46] Q. Zhu, Y. Zhong, B. Zhao, G.-S. Xia, and L. Zhang, "Bag-of-visual-words scene classifier with local and global features for high spatial resolution remote sensing imagery," *IEEE Geosci. Remote Sens. Lett.*, vol. 13, no. 6, pp. 747–751, 2016.
- [47] X. Wang, L. Xie, C. Dong, and Y. Shan, "Real-ESRGAN: Training real-world blind super-resolution with pure synthetic data," in *Proc. IEEE/CVF Int. Conf. Comput. Vis. (ICCV)*, 2021, pp. 1905–1914.
- [48] M. Kang, J. Y. Zhu, R. Zhang *et al.*, "Scaling up GANs for text-to-image synthesis," in *Proc. IEEE/CVF Conf. Comput. Vis. Pattern Recognit. (CVPR)*, 2023, pp. 10124–10134.
- [49] OpenAI, "GPT-4 technical report," *arXiv:2303.08774*, 2023.
- [50] R. Rombach, A. Blattmann, D. Lorenz, P. Esser, and B. Ommer, "High-resolution image synthesis with latent diffusion models," in *Proc. IEEE/CVF Conf. Comput. Vis. Pattern Recognit. (CVPR)*, 2022, pp. 10684–10695.
- [51] R. Khanna, S. Thakur, and R. Khurana, "Satellite imagery augmentation using latent diffusion for improved classification performance," *Remote Sens.*, vol. 15, no. 4, p. 923, 2023.
- [52] E. J. Hu, Y. Shen, P. Wallis *et al.*, "LoRA: Low-rank adaptation of large language models," *arXiv:2106.09685*, 2022.
- [53] L. Zhang and M. Agrawala, "Adding conditional control to text-to-image diffusion models," in *Proc. IEEE/CVF Int. Conf. Comput. Vis. (ICCV)*, 2023, pp. 3836–3847.
- [54] A. Toker, H. Kaplan, and S. Aksoy, "Diffusion-based data augmentation for remote sensing image segmentation," *Remote Sens.*, vol. 16, no. 2, p. 245, 2024.
- [55] M. Tang, C. Xu, Y. Li, and Q. Zhao, "Controlled diffusion models for realistic aerial image generation," *IEEE J. Sel. Top. Appl. Earth Obs. Remote Sens.*, vol. 17, pp. 198–212, 2024.
- [56] Y. Xiong, Z. Li, Y. Chen *et al.*, "Efficient Deformable ConvNets: Rethinking dynamic and sparse operator for vision applications," in *Proc. IEEE/CVF Conf. Comput. Vis. Pattern Recognit. (CVPR)*, 2024, pp. 5652–5661.
- [57] H. Li, Y. Zhang, Y. Zhang, H. Li, and L. Sang, "DCNv3: Towards next generation deep cross network for CTR prediction," *arXiv:2407.13349*, 2024.
- [58] Y. Wang, Q. Chen, Y. Xiong *et al.*, "InternImage: Exploring large-scale vision foundation models with deformable convolutions," *arXiv:2211.05778*, 2022.
- [59] J. Deng, W. Dong, R. Socher, L.-J. Li, K. Li, and L. Fei-Fei, "ImageNet: A large-scale hierarchical image database," in *Proc. IEEE Conf. Comput. Vis. Pattern Recognit. (CVPR)*, 2009, pp. 248–255.
- [60] T.-Y. Lin, M. Maire, S. Belongie *et al.*, "Microsoft COCO: Common objects in context," in *Proc. Eur. Conf. Comput. Vis. (ECCV)*, 2014, pp. 740–755.
- [61] B. Zhou, H. Zhao, X. Puig *et al.*, "Scene parsing through ADE20K dataset," in *Proc. IEEE Conf. Comput. Vis. Pattern Recognit. (CVPR)*, 2017, pp. 633–641.
- [62] A. Dosovitskiy, L. Beyer, A. Kolesnikov *et al.*, "An image is worth 16x16 words: Transformers for image recognition at scale," *arXiv:2010.11929*, 2020.

- [63] S. Chen, J. Liang, J. Zhu, and X. Tian, “New methods for lunar impact crater detection based on YOLO v7 with deformable ConvNets,” in *Proc. IEEE Int. Conf. Electrical, Automation and Computer Engineering (ICEACE)*, 2023, pp. 123–127.
- [64] M. Bińkowski, A. Letcher, A. Kumar *et al.*, “Demystifying MMD GANs,” *arXiv:1801.01401*, 2018.
- [65] A. Li, Z. Wang, H. Zhang *et al.*, “PID: Prompt-independent data protection against latent diffusion models,” *arXiv:2406.15305*, 2024.
- [66] C. Qin, S. Zhang, N. Yu, Y. Feng, X. Yang, Y. Zhou, H. Wang, J. C. Niebles, C. Xiong, S. Savarese *et al.*, “Unicontrol: A unified diffusion model for controllable visual generation in the wild,” *arXiv:2305.11147*, 2023.
- [67] Z. Dong, Y. Sun, T. Liu, W. Zuo, Y. Gu, “EarthMapper: Visual Autoregressive Models for Controllable Bidirectional Satellite-Map Translation,” *arXiv:2504.19432*, 2025.
- [68] J. Hu, L. Mou, and X. X. Zhu, “Unsupervised domain adaptation using a teacher–student network for cross-city classification of Sentinel-2 images,” *Int. Arch. Photogramm. Remote Sens. Spatial Inf. Sci.*, vol. XLIII-B2-2020, pp. 1569–1574, 2020.
- [69] D. M. W. Powers, “Evaluation: From precision, recall and F-measure to ROC, informedness, markedness and correlation,” *arXiv:2010.16061*, 2020.
- [70] I. Loshchilov and F. Hutter, “Decoupled weight decay regularization,” *arXiv:1711.05101*, 2017.
- [71] Y. C. Zhang, J. P. Gao, and H. L. Zhou, “Breeds classification with deep convolutional neural network,” in *Proc. 12th Int. Conf. Mach. Learn. Comput.*, 2020, pp. 145–151.
- [72] K. He, X. Zhang, S. Ren, and J. Sun, “Deep residual learning for image recognition,” in *Proc. IEEE Conf. Comput. Vis. Pattern Recognit.*, 2016, pp. 770–778.
- [73] M. Sandler, A. Howard, M. Zhu, A. Zhmoginov, and L.-C. Chen, “Mobilenetv2: Inverted residuals and linear bottlenecks,” in *Proc. IEEE Conf. Comput. Vis. Pattern Recognit.*, 2018, pp. 4510–4520.
- [74] S. Ren, K. He, R. Girshick, and J. Sun, “Faster r-cnn: Towards real-time object detection with region proposal networks,” in *Adv. Neural Inf. Process. Syst.*, vol. 28, 2015.
- [75] K. Simonyan and A. Zisserman, “Very deep convolutional networks for large-scale image recognition,” *arXiv preprint arXiv:1409.1556*, 2014.
- [76] M. Everingham, L. Van Gool, C. K. I. Williams, J. Winn, and A. Zisserman, “The Pascal visual object classes (VOC) challenge,” *Int. J. Comput. Vis.*, vol. 88, no. 2, pp. 303–338, 2010.
- [77] T.-Y. Lin, M. Maire, S. Belongie, J. Hays, P. Perona, D. Ramanan, P. Dollár, and C. L. Zitnick, “Microsoft COCO: Common objects in context,” in *Proc. Eur. Conf. Comput. Vis.*, 2014, pp. 740–755.
- [78] J. L. Hennessy and D. A. Patterson, *Computer Architecture: A Quantitative Approach*, 5th ed. San Mateo, CA, USA: Morgan Kaufmann, 2011.
- [79] L.-C. Chen, G. Papandreou, F. Schroff, and H. Adam, “Rethinking atrous convolution for semantic image segmentation,” *arXiv preprint arXiv:1706.05587*, 2017.
- [80] H. Fan, S. Liu, M. Ferianc, H.-C. Ng, Z. Que, S. Liu, X. Niu, and W. Luk, “A real-time object detection accelerator with compressed SSDLite on FPGA,” in *Proc. Int. Conf. Field-Programm. Technol. (FPT)*, 2018, pp. 14–21.